IEEE Robotics & Automation Magazine (RAM) paper, presented at ICRA 2026, Vienna, Austria. Cite as RAM paper.

Transendoscopic Telerobotic System

Heterogeneous Flexible Manipulators for Bimanual Endoscopic Submucosal Dissection

By Huxin Gao, Xiaoxiao Yang, Tao Zhang, Xiao Xiao, Changsheng Li, Max Q.-H. Meng, Xiuli Zuo, Yanqing Li, and Hongliang Ren

Endoscopic submucosal dissection (ESD) is an effective technique to resect early cancers in the gastrointestinal (GI) tract. Bimanual telerobotic manipulation is an approach to performing ESD intuitively and efficiently, which requires two robotic instruments with flexibility, stiffness, dexterity, and accuracy. In detail, specific elementary ESD action requires a corresponding priority of the above properties. In this article, we propose the first heterogeneous flexible manipulators (HFMs) for bimanual ESD, which can take advantage of different mechanical structures toward specific ESD actions. The grasping instrument employs a serial articulated manipulator (SAM) to perform multidirectional (relatively higher dexterity) and stable (relatively higher stiffness) traction for better submucosal visualization. The electrosurgical instrument utilizes a parallel-continuum wrist (PCW) to execute safe (higher-accuracy) tissue dissection. Both HFMs have sufficient flexibility (i.e., lower bending stiffness values than the endoscope) to go through the flexible endoscopic working channels. Based on the HFMs, we establish a transendoscopic telerobotic system. The kinematics of the SAM and PCW are built in the endoscope frame using the Denavit–Hartenberg (DH) method and the Cosserat rod method, respectively. Through simulation, the SAM is proved to have higher dexterity than the PCW, and they share enough workspace to cover lesions with diameters over 30 mm. The HFM-based robotic system is validated to perform efficient and safe ESD through ex vivo tests with tiered difficulty. The HFMs may offer a feasible strategy to develop robots for more forms of surgery by leveraging different mechanical structures for specific ESD actions.

Digital Object Identifier 10.1109/MRA.2025.3616737

IEEE Robotics & Automation Magazine (RAM) paper, presented at ICRA 2026, Vienna, Austria. Cite as RAM paper

INTRODUCTION

ESD is a well-developed therapeutic technique to resect lesions in the GI tract [1]. It enables en bloc removal of large (diameter >20 mm) and deep (in nonepithelial tissues) GI lesions. The en bloc resection can improve the accuracy of postoperative pathological examination. The rate of en bloc resection generally depends on the clear exposure and traction of submucosa and accurate tissue dissection. Traditional ESD highly relies on endoscopists' skills due to the nonintuitive manipulation of flexible endoscopes. Besides, the conventional traction device (transparent caps attached to the endoscope tip) is limited in providing a clear submucosal view. However, the implementation of this method highly relies on endoscopic skills due to the limited degrees of freedom (DoF) of ESD instruments: translation and rotation. Therefore, plenty of mechanical structures have been developed to improve the dexterity of surgical instruments, and telerobotic technology is used to enhance operative intuition, typically Endowrist and the da Vinci system. These virtually move a surgeon's dexterous wrists/hands to the surgical site [2]. For ESD, flexibility is a fundamental property [3] that enables robotic instruments to access any part of the GI tract. On this premise, the distal instruments for different ESD actions,[1] as reported in Table 1, have a specific priority of the following properties: stiffness, dexterity, and accuracy. In detail, instruments for tissue traction should possess higher dexterity and stiffness to execute multidirectional and stable traction, respectively, for a clear submucosal view. Instruments for tissue cutting should have better manipulative accuracy to perform safe submucosal dissection.

To adapt to the flexible GI tract, flexible structures should be employed in the transmission and end effector of an ESD instrument. The transmission commonly employs flexible tubes or wires. The flexible structures can be generally divided into articulated structures and continuum structures. The articulated structures have serial and parallel forms. Serial articulated structures typically feature rigid links consecutively connected by joints, such as rolling friction joints [5] and sliding hinged joints [6] (according to the classification in [7]). Parallel articulated structures are constructed by parallelly arranged transmission chains, such as prismatic–spherical–revolute chains [8] and prismatic–universal chains [9]. These parallel structures can potentially improve the positioning accuracy and stiffness of the manipulator's end effector, but the rigid articulated joints in each transmission chain restrict the development of transendoscopic miniature manipulators.

Continuum structures in the surgical field have achieved great progress in the last two decades, and they can be classified into the following three types. First, backbone-based continuum structures use single central or multiple peripheral elastic rods [10] as bending elements and are driven by tendons. Their miniaturization will increase the difficulty of assembly and dramatically decrease stiffness. Second, concentric continuum structures [2] adjust the end effector's pose through mutual translation and rotation of inner and outer precurved tubes or push–pull tubes [11]. However, the long curved working channels cannot transmit torque effectively from the proximal to the distal side, causing snapping problems [12]. Third, parallel-continuum structures [13] change the transmission chains in parallel articulated structures to elastic rods, which can overcome the size limitation but still maintain accuracy and stiffness [14].

Different instrument structures exhibit distinct mechanical properties, making them uniquely suited for specific ESD actions. As shown in Table 1, clinical ESD requirements suggest that serial articulated structures, with their high stiffness, are suitable for tissue traction, whereas parallel-continuum structures can offer higher accuracy and stiffness for tissue dissection compared to other continuum structures. Thus, the optimal approach can involve selecting instrument structures based on the specific demands of each ESD action.

Our previous work developed two kinds of novel robotic instruments, a SAM [15] and a PCW [16]. The telerobotic system consists of two manipulators with the same mechanical structure to handle all ESD actions. While our prior contributions focused on designing and validating various new mechanical structures, this article aims to combine heterogeneous manipulators in one surgical robotic system and validate its feasibility in ESD procedures. Our new contributions are summarized as follows:

1) We develop the first HFMs for bimanual ESD, as depicted in Figure 1, combining a SAM (diameter: 3.5 mm) for tissue lifting and a PCW (diameter: 2.5 mm) for tissue dissection.
2) Based on the HFMs, we build a transendoscopic telerobotic system using a commercial flexible endoscope (diameter: 11.8 mm) with two working channels (diameters: 3.8 and 2.8 mm). The feasibility and performance of the system are validated by 16 ex vivo tests.
3) This article demonstrates the feasibility of combining instruments based on heterogeneous structures to develop surgical robotic systems, which has not been previously reported in the literature. This can leverage individual advantages of heterogeneous structures to improve the efficacy of robotic surgery.

TABLE 1. The HFMs for bimanual ESD.

ESD TASK	ESD ACTION	ACTION REQUIREMENTS	HFMS STRUCTURE	STRUCTURE ADVANTAGES
Submucosal dissection	Dissection	Safe	PCW	High accuracy
	Traction	Stable, multidirectional	SAM	High stiffness and dexterity

---

[1] Level of granularity [4]: ESD indicates high-level operation. ESD consists of four sequential tasks: marking, injection, circumferential incision, and submucosal dissection. Each task can be divided into some low-level actions.

IEEE Robotics & Automation Magazine (RAM) paper, presented at ICRA 2026, Vienna, Austria. Cite as RAM paper.

The rest of the article is organized as follows. The "HFMs Design" and "Kinematics" sections introduce the design and kinematics of the HFMs in detail. Then, simulations are conducted in the "Property Analysis" section to analyze the cooperation of the SAM and the PCW. In the "Performance Validation" section, the complete robotic system is established and validated in ex vivo tests. Finally, we conclude the article with limitations and discuss future work.

HFMS DESIGN

In ESD, submucosal dissection is the most important phase, consisting of two elementary surgical actions (see Figure 1): 1) stable and multidirectional tissue traction and 2) safe tissue dissection. To better perform bimanual ESD, the design of HFMs should satisfy the following requirements:

1) *Working property priority*: Flexibility, stiffness, dexterity, and accuracy are four important working properties for ESD instruments. To better perform ESD, HFMs for specific ESD actions should leverage individual advantageous mechanical properties.
2) *Transendoscopic dimension*: Compared to an externally mounted tube on a single-channel endoscope, transendoscopic instruments can reduce the overall diameter of the insertion part and be comfortable in a patient's GI tract. The commonly used dual-channel endoscopes are generally around 1,200 mm long from the entry to the exit and are around 2.8 and 3.8 mm in channel diameter. Therefore, each manipulator should satisfy this transendoscopic dimension.
3) *Workspace*: The en bloc resection of lesions with diameters over 20 mm generally resorts to ESD [1]. Besides, the lesions may be distributed at the GI tract with different orientations. Therefore, each manipulator's workspace should cover a column space with a diameter of over 20 mm and a length of over 20 mm.
4) *Instrument functionality*: The manipulators for lifting and cutting should be mounted with forceps and an electric knife as the end effectors, respectively.

In our previous work, we developed a variable-stiffness SAM [15], [17] and a PCW [16]. The HFMs for ESD have four important working properties: flexibility, stiffness, dexterity, and accuracy. For flexibility, the bending stiffness values of the SAM and PCW transmissions are 6.9 and 3.6 mN · mm/rad, significantly smaller than that of the endoscope (17 mN · mm/rad). This allows both the SAM and PCW to smoothly pass through and work within the flexible endoscopic working channels. For stiffness, the SAM can increase stiffness to 0.71 N/mm [17] after insertion, which is higher than the PCW stiffness range of 0.26–0.59 N/mm [16]. Therefore, the SAM can perform more stable tissue traction than the PCW. For accuracy, the PCW can achieve an average motion tracking accuracy of 0.52 mm [16], which is capable of precise tissue cutting. In this section, the HFMs' dexterity is analyzed in detail. Besides, their cooperative workspace is simulated to evaluate collaboration. To leverage their relatively outstanding properties, we propose HFMs for bimanual ESD.

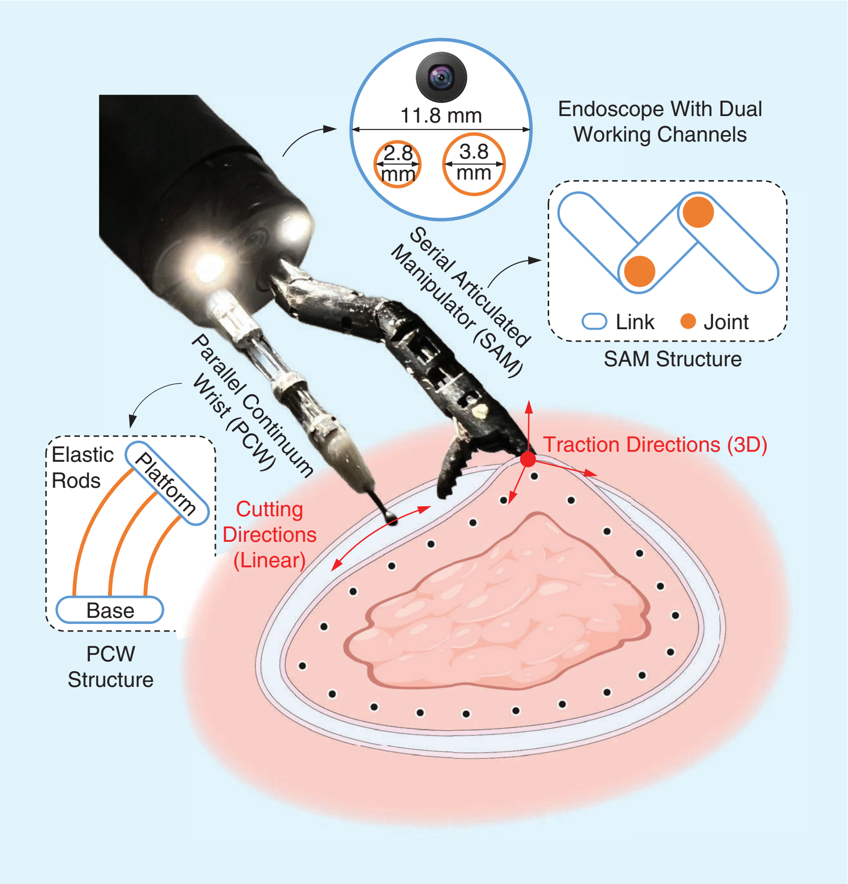

FIGURE 1. The HFMs, consisting of the SAM and PCW, for bimanual ESD. The HFMs pass through two working channels (around 2.8 and 3.8 mm) of commercial flexible endoscopes to perform ESD procedures. While the SAM is lifting the mucosa flap multidirectionally for better submucosal visualization, the PCW is cutting the submucosa (connective tissue) to remove the lesion. The structural principles of the SAM and PCW are illustrated in two insets.

SAM

To satisfy the design requirements, the SAM with a variable-stiffness mechanism is upgraded from the original robotic prototype [17] to the transendoscopic version, as displayed in Figure 2. The SAM system consists of a distal manipulator with a serial articulated structure, a tendon–sheath transmission, and a proximal driver. In detail,

IEEE Robotics & Automation Magazine (RAM) paper, presented at ICRA 2026, Vienna, Austria. Cite as RAM paper.

there are eight link–transmission–actuator modules: a translation module, a rotation module, two abduction/adduction modules, two abduction/adduction stiffness modules, a wrist module, and a forceps module.

DISTAL MANIPULATOR

The SAM, illustrated in Figure 2(b), needs to execute tissue traction, and its end effector is a pair of forceps with sharp teeth. Compared to the previous version, one of the forceps is changed to a link with teeth to form an effective wrist DoF. The diameter and length of the SAM are 3.5 and 30 mm, respectively. The SAM consists of five links: base, link 1, link 2, link 3, and forceps. The former three links constitute four identical DoF/joints: translation $\mathcal{A}$ and rotation $\mathcal{B}$ of the whole manipulator, abduction joint $\mathcal{B}$, and adduction joint $\mathcal{D}$. The latter two links form a wrist joint $\mathcal{E}$ and a grasping joint $\mathcal{F}$. The DoF $\mathcal{A}$ and $\mathcal{B}$ are driven by a torque coil (Torque Coil, Asahi Intecc) with an outer diameter of 3.5 mm, and other DoF are driven by cables with a diameter of 0.2 mm. For the joints $\mathcal{C}$ and $\mathcal{D}$, each one is joined by mutually fitting curved pieces and is actuated by two motors to enable variable stiffness [15]. Each end effector's joint is actuated by one motor. The wrist joint is joined by the curved interfaces of link 2 and link 3. The forceps' joint is pinned by a shaft.

TENDON–SHEATH TRANSMISSION

The tendon–sheath mechanism (TSM) [18] is adopted for transmission, as in Figure 2(c). Its length is extended to 1,380 mm, and its outer diameter is reduced to 3.5 mm. The transmission structure consists of a torque coil and eight tendon–sheath pairs [see the inset in Figure 2(a)]. The torque coil is utilized to transfer the translational force and rotational torque to the base of the SAM. The tendon and sheath employ wire rope (diameter: 0.2 mm) and a stainless steel capillary (inner diameter: 0.3 mm; thickness: 0.1 mm), respectively. The distal end of each sheath is fixed at the base.

PROXIMAL DRIVER

The driver is optimized to reduce the size and weight of the whole robotic system and accelerate instrument exchange during operation. The driver, with a volume of $300 \times 157 \times 75\ \text{mm}^3$, includes eight actuation units: one translation actuator, one rotation actuator, and six identical tendon–sheath actuators for other DoF and stiffness tuning. The rotation actuator vertically mounts a gear pair with a reduction ratio of 50 to rotate the torque coil, which is fixed in the gear. The translation actuator utilizes a lead screw (lead: 0.5 mm) to move the distal manipulator forward and backward. Each tendon–sheath actuator horizontally arranges a pair of a worm wheels and a gear (reduction ratio: 50) to rotate a pulley. To exchange instruments rapidly, the driver is divided into an upper layer and a lower layer. The lower layer mainly contains the above actuators. The upper layer is connected to the distal manipulator via a TSM transmission. The two layers are connected by six vertical shafts and are fixed by six rotary knobs.

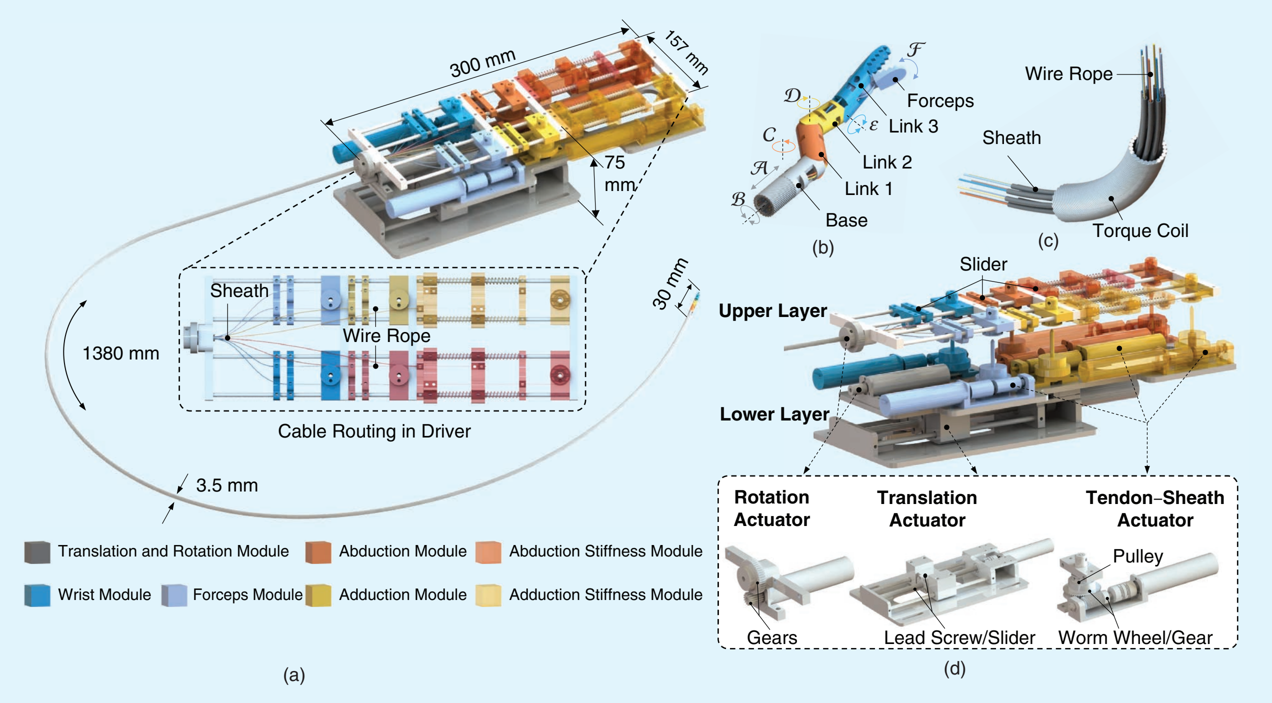

FIGURE 2. 3D models of the designed GESR system. (a) The GESR model. The detailed cable routing is plotted in a dashed box. To clearly illustrate the relationship between the manipulator and driver, each link–transmission–actuator module is rendered in the same color. The stiffness modules utilize lighter colors for their corresponding module. (b) The manipulator. (c) The transmission. (d) The driver. Models of the actuation units are displayed in the bottom box.

IEEE Robotics & Automation Magazine (RAM) paper, presented at ICRA 2026, Vienna, Austria. Cite as RAM paper.

PCW

The detailed PCW mechanism can be found in our previous work [16]. Here, the PCW system is concisely introduced.

DISTAL WRIST

The PCW, with a length of 21 mm and a diameter of 2.5 mm, consists of a base, a parallel-continuum structure, and a platform assembled with an electric knife. It has 3 DoF, as exhibited in Figure 3: translation $\mathcal{G}$, pitch $\mathcal{H}$, and yaw $\mathcal{I}$. DoF $\mathcal{G}$ is driven by the polytetrafluoroethylene (PTFE) tube and internal sheaths. The DoF $\mathcal{H}$ and $\mathcal{I}$ are formed by a four-nickel–titanium (NiTi)-rod parallelly arranged structure. The platform is integrated with an insulating part made of polyether ether ketone to fix an electric knife. The electric knife's metal cable passes through an inner PTFE tube to insulate itself from the metal base and platform. Besides, the distance of the base and platform is kept at 5 mm to trade off the DoF $\mathcal{H}$ and $\mathcal{I}$ displacement and the wrist's stiffness.

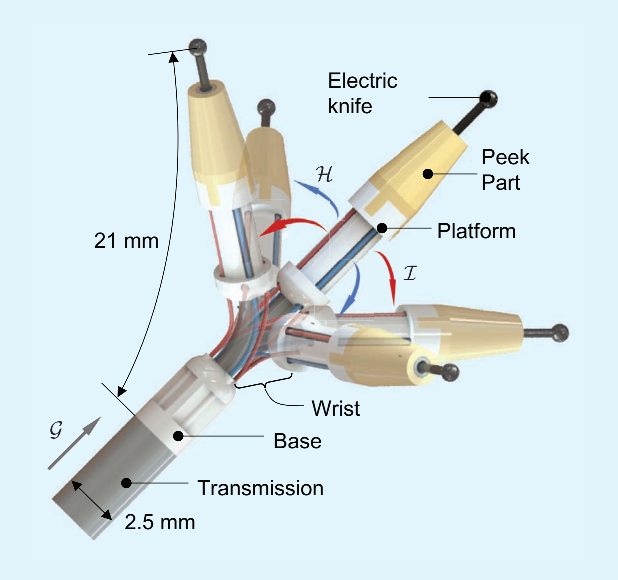

FIGURE 3. The designed PCW. Two bending DoF, $\mathcal{H}$ and $\mathcal{I}$, are displayed with blue and red arrows, respectively.

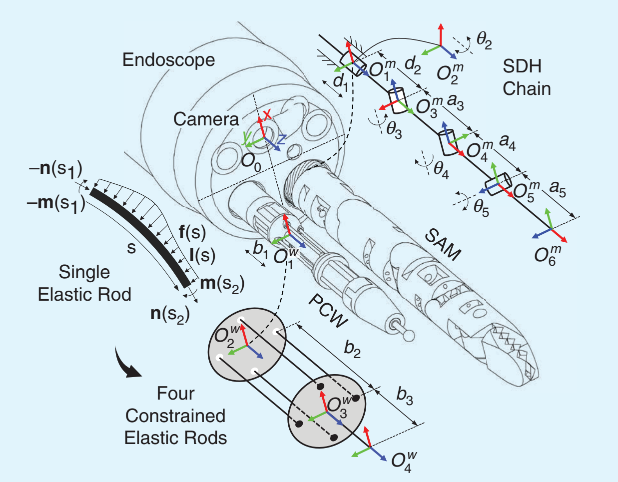

FIGURE 4. The kinematics of the HFMs. The frame of HFMs O_0 is fixed on the center of the distal camera. Upper right corner: a kinematical diagram of the SAM relative to its own base. Lower left: a kinematical diagram of the PCW relative to its own base. A single flexible link is illustrated by the Cosserat rod model, and then four flexible links are constrained on the platform.

TENDON–SHEATH TRANSMISSION

The PCW also employs a TSM. The tendon and sheath are a NiTi rod (diameter: 0.2 mm) and stainless steel capillary (inner diameter: 0.3 mm; thickness: 0.1 mm). Compared to the wire rope used in the SAM, a NiTi rod can provide push–pull force. The outer tube uses PTFE for electric insulation and force transmission from the proximal driver to the PCW base.

PROXIMAL DRIVER

The PCW driver utilizes linear motion stages to exert effective push–pull force on the NiTi rods and transmission. To reduce the size of the PCW driver, each DoF $\mathcal{H}/\mathcal{I}$ of the wrist is actuated by one motor. Between the NiTi rod and the motor, the transmission structure utilizes a linear motion stage with a twin lead screw, which provides opposite motions. The translation DoF $\mathcal{H}$ directly resorts to a linear motion stage to move the transmission structure.

KINEMATICS

In this section, we first establish the kinematics of the SAM and PCW and then transform them into the coordinate system of the endoscopic camera as the HFMs' kinematics.

SAM

JOINT SPACE TO TASK SPACE

The SAM is connected by five rigid links. We directly use the standard DH (SDH) method to establish the kinematics. The end-effector frame O_6^m is located at the center of the forceps. Besides, the DoF $\mathcal{A}$ and $\mathcal{B}$ are transferred from the torque coil to the SAM base. For convenience, the base frame O_1^m is set at the interface of the base and the torque coil. The entire kinematic chain of the SAM is illustrated in the upper-right corner of Figure 4. The vector $q^m = [d_1, \theta_2, \theta_3, \theta_4, \theta_5]$ corresponds to the actuation of the DoF $\mathcal{A} - \mathcal{E}$. The end-effector's pose with respect to the base, the homogeneous transformation matrix ${}_6^1T^m(q^m)$, can be computed by the following equation with the SDH parameters listed in Table 2:

TABLE 2. The DH parameters for the manipulator.

i	α_i	a_i	d_i	θ_i	RANGE
1	0	0	d_1	0	0 ~ 30
2 (base)	$\pi/2$	0	6.6	$\theta_2 + \pi/2$	$-\pi \sim \pi$
3 (link 1)	0	7.5	0	$\theta_3 + \pi/2$	$0 \sim \pi/3$
4 (link 2)	$\pi/2$	6.2	0	θ_4	$-\pi/3 \sim 0$
5 (forceps)	0	8.2	0	θ_5	$-\pi/3 \sim \pi/3$

IEEE Robotics & Automation Magazine (RAM) paper, presented at ICRA 2026, Vienna, Austria. Cite as RAM paper.

$$
{}^{1}_{6}T^{m} = {}^{1}_{2}T^{m}\,{}^{2}_{3}T^{m}\,{}^{3}_{4}T^{m}\,{}^{4}_{5}T^{m}\,{}^{5}_{6}T^{m},
$$

$$
{}^{i-1}_{\;\;i}T^{m} = \begin{bmatrix} \cos\theta_i & -\sin\theta_i\cos\alpha_i & \sin\theta_i\sin\alpha_i & a_i\cos\theta_i \\ \sin\theta_i & \cos\theta_i\cos\alpha_i & -\cos\theta_i\sin\alpha_i & a_i\sin\theta_i \\ 0 & \sin\alpha_i & \cos\alpha_i & d_i \\ 0 & 0 & 0 & 1 \end{bmatrix}. \quad (1)
$$

ACTUATION SPACE TO JOINT SPACE

The analytical functions from the task space to the joint space can be easily derived from (1), whose process is similar to [17]. Then, to map the joint space to the actuation space, the geometrical relationship between the joint actuation and its driving cables can be obtained from its structural design [19]. However, because of friction, backlash, hysteresis, and other problems in the physical system, the above mapping tends to be inaccurate. Additionally, the variable-stiffness mechanism results in more severe and complex nonlinear phenomena. Therefore, we propose a new data-driven method, the stiffness-dependent modified generalized Prandtl–Ishlinski (MGPI) model [17], to construct the relationship between motor input (actuation space) a^m and the SAM's joint (joint space) q^m. This can be formulated as $q^m = \mathrm{MGPI}(a^m)$, where MGPI indicates the stiffness-dependent hysteresis model and has an analytical inverse function to support real-time control. The hysteresis compensation uses feedforward control, where the inverse hysteresis model is cascaded with the actual hysteresis to equalize the output with the desired output. More details can be found in supplementary material available at https://doi.org/10.1109/MRA.2025.3616737 and in our previous work [17].

PCW

SINGLE ELASTIC ROD

The kinematic modeling of the PCW starts with a single elastic rod using the Cosserat rod method. The pose of ith elastic rod from the PCW base is expressed as a function of rod length $s_i : T_i(s) = \begin{bmatrix} R_i(s_i) & p_i(s_i) \\ 0 & 1 \end{bmatrix}, s_i \in [0, L_w]$, where $R_i(s_i)$ and $p_i(s_i)$ are the orientation and position of the ith rod along the rod length. Here, L_w is the wrist length and equals the summation of initial wrist length L'_w and rod actuation $q_i^w : L_w = L'_w + q_i^w$, and $q^w = [q_1^w, q_2^w, q_3^w, q_4^w]$ has four elements, which, because of the antagonistic driver, should satisfy

$$
q_3^w = -q_1^w, q_4^w = -q_2^w, q_i^w \in [-1.7, 1.7]. \quad (2)
$$

The derivatives, $\dot{p}$ and $\dot{R}$, relative to s_i can be derived from the linear, v_i, and angular, u_i, rates of change in the body frame, as follows:

$$
\dot{p}_i = R_i v_i, \;\; \dot{R}_i = R_i \hat{u}_i \quad (3)
$$

where ^ indicates the skew-symmetric matrix of a vector.

The internal force n_i and moment m_i are related to deformation v_i and u_i via linear constitutive equations and expressed in the base frame O_2^w.

$$
\begin{aligned} n_i &= R_i K_{\mathrm{se}}(v_i - v'_i), K_{\mathrm{se}} = \mathrm{diag}(AG, AG, AE) \\ m_i &= R_i K_{\mathrm{bt}}(u_i - u'_i), K_{\mathrm{bt}} = \mathrm{diag}(EI, EI, JG) \end{aligned} \quad (4)
$$

where K_{se} and K_{bt} are diagonal stiffness matrices describing shear/elongation items and bending/torsion items, respectively; E and G are the Young's modulus and the shear modulus of the rod material, respectively; A is the area of the rod cross section; I is the moment of inertia of the rod (equal in the x- and y-axes); J is the polar moment along the z-axis; and $'$ indicates the initial value ($v'_i = [0, 0, 1]^T, u'_i = [0, 0, 0]^T$).

Assuming the distributed force f_i and moment l_i along the rod, the equilibriums of the Cosseart rod are established.

$$
\dot{n}_i = -f_i, \; \dot{m}_i = -\dot{p}_i \times n_i - l_i \quad (5)
$$

where $\dot{n}_i$ and $\dot{m}_i$ are the derivatives of the force and moment with respect to the rod length.

Equations (3)–(5) form the system of ordinary differential equations (ODEs) about functions $[n_i, m_i, p_i, R_i]$ with respect to s_i. To numerically solve ODEs with initial guess $[n_i(0), m_i(0), p_i(0), R_i(0)]$ at high accuracy and low computational cost, one of the high-order Runge–Kutta methods, called the *Dormand–Prince method*, is implemented by the ode45 solver in MATLAB.

CONSTRAINT OF PARALLEL STRUCTURE

Four rods are arranged in parallel and fixed on the PCW platform. As a result, static equilibrium and geometrical constraints are exerted on the platform ($s_i = L_w$ at the end of the rods). The former describes the relationships between the internal force/moment $[n_i(L_w)/m_i(L_w)]$ and the external force/moment F/M.

$$
\begin{aligned} &\sum_{i=1}^{4} [n_i(L_w)] - F = 0 \\ &\sum_{i=1}^{4} [p_i(L_w) \times n_i(L_w) + m_i(L_i)] + {}^{2}_{3}p^{w} \times F - M = 0 \end{aligned} \quad (6)
$$

where ${}^{2}_{3}p^{w}$ is the position of the PCW platform frame O_3^w.

Besides, the geometrical constraints contain positional and orientational components, as follows:

$$
\begin{aligned} {}^{2}_{3}p^{w} + {}^{2}_{3}R^{w}\rho_i - p_i(L_w) = 0, \;\; i = 1, \ldots, 4 \\ [\log(R_i(L_w)^{T}\,{}^{2}_{3}R^{w} R_{\alpha_i})]^{\vee} = 0, \;\; i = 1, \ldots, 4 \end{aligned} \quad (7)
$$

where $\log()$ maps $SO(3)$ to $\mathfrak{so}(3)$; $\vee$ indicates the inverse operation of the skew-symmetric matrix; ρ_i and R_{α_i} are the position and orientation of the distal frame of the rod $R_i(L_w)$, the rod expressed in the platform frame O_3^w; and ${}^{2}_{3}R^{w}$ is the orientation of the PCW platform frame O_3^w.

The constraints in (6) and (7) represent the distal boundary conditions that couple the four elastic rods at $s_i = L_w$, forming a boundary value problem (BVP). To solve this BVP, the shooting method is employed, converting the BVP into an initial value problem and iteratively refining the initial guesses of the four rods (in the last section) until the distal boundary conditions are satisfied. Once solved, the pose of the PCW platform, ${}^{2}_{3}T^{w} = \begin{bmatrix} {}^{2}_{3}R^{w} & {}^{2}_{3}p^{w} \\ 0 & 1 \end{bmatrix}$, can be computed.

ACTUATION SPACE TO TASK SPACE

Besides the bending motion provided by the parallel-continuum structure, translational motion is also exerted on the PCW base to enlarge the workspace. Then, the electric knife is fixed on the PCW platform. Consequently, the pose of the knife tip is expressed in the base frame O_1^w.

$$
\begin{aligned}
&{}^{1}_{4}T^{w} = {}^{1}_{2}T^{w}\,{}^{2}_{3}T^{w}\,{}^{3}_{4}T^{w}, \\
&{}^{1}_{2}T^{w} = \begin{bmatrix} \boldsymbol{I} & [0,0,b_1]^T \\ 0 & 1 \end{bmatrix}, {}^{3}_{4}T^{w} = \begin{bmatrix} \boldsymbol{I} & [0,0,b_3]^T \\ 0 & 1 \end{bmatrix}
\end{aligned}
\tag{8}
$$

where $\boldsymbol{I}$ is a 3×3 identity matrix, b_1 is the translation variable of the PCW, and b_3 is the distance between the knife tip frame O_4^w and the platform frame O_3^w.

HFMs

The SAM and PCW cooperate as HFMs under the geometrical constraint of two endoscopic working channels. Hence, the relationships of the HFMs, ${}^{0}_{6}T^{m}$ and ${}^{0}_{4}T^{w}$, can be constructed on the frame O_0, the center of the camera, as follows:

$$
\begin{aligned}
&{}^{0}_{6}T^{m} = {}^{0}_{1}T^{m}\,{}^{1}_{6}T^{m}, {}^{0}_{4}T^{w} = {}^{0}_{1}T^{w}\,{}^{1}_{4}T^{w}, \\
&{}^{0}_{1}T^{m} = \begin{bmatrix} {}^{0}_{1}R^{m}_{z} & {}^{0}_{1}p^{m} \\ 0 & 1 \end{bmatrix}, {}^{0}_{1}T^{w} = \begin{bmatrix} {}^{0}_{1}R^{w}_{z} & {}^{0}_{1}p^{w} \\ 0 & 1 \end{bmatrix}
\end{aligned}
\tag{9}
$$

where ${}^{0}_{1}T^{m}$ and ${}^{0}_{1}T^{w}$ are transformation matrices of the frames O_1^m and O_1^w with respect to the frame O_0, ${}^{0}_{1}R^{m}_{z}$ and ${}^{0}_{1}R^{w}_{z}$ are the initial rotation matrix of the SAM and PCW bases around the z-axis of the frame O_0, and ${}^{0}_{1}p^{m}$ and ${}^{0}_{1}p^{w}$ are initial positions of the SAM and PCW bases in the frame O_0.

PROPERTY ANALYSIS

In this section, the cooperative dexterity and workspace are analyzed.

DEXTERITY

The SAM needs to adjust the motion direction (linear motion in 3D space) to exert sufficient traction on the submucosa and expose it clearly in the endoscopic view. Simultaneously, the PCW follows the borderline of the submucosa and muscularis (linear motion in 2D space) to perform dissection. Therefore, tissue traction and cutting define high- and low-dexterity requirements for the SAM and PCW, respectively. Here, the ratio of the longest semiaxis to the shortest semiaxis of the manipulability ellipsoid in (1) is utilized as a metric to evaluate the dexterity of the SAM and PCW. Besides, traction and cutting generally belong to linear motions, so the dexterity metric μ employs the translational velocity ellipsoid.

$$
\mu(q) = \sqrt{\frac{\mathrm{eig}_{\max}(J_v J_v^T)}{\mathrm{eig}_{\min}(J_v J_v^T)}}, \mu \in [1, \infty)
\tag{10}
$$

where q is the actuation values of the SAM or PCW; J_v is the linear Jacobian, which can be acquired by finite-difference approximation based on kinematics; and "eig" computes a matrix's eigenvalues. The metric μ approaching 1 means the manipulator has better motion capability in all directions, signifying greater dexterity; μ^m and μ^w indicate the SAM's and PCW's dexterity, respectively.

The dexterity distributions of the SAM and PCW are presented in Figure 5. First, the best dexterity metric value μ^m of the SAM is 4.44, which is nearly a quarter of the PCW's value of 16.94. This shows that the SAM can perform better 3D motion than the PCW. Second, the PCW's ellipsoids often approximate ellipses compared with the SAM's ellipsoids, which means that the PCW prefers 2D motion. Third, two ellipsoids with high dexterity values show that worse linear motion often happens to the SAM with the adduction DoF $\mathcal{D}$ of 0° [e.g., $\mu^m([0, 0, pi/4, 0, 0]) = 37.11$)] and to the PCW with the maximum bending angle of 90° [e.g., $\mu^w([0, 0, 1.7, 0, -1.7]) = 229.01$)]. This result points out improper configurations for the HFMs. Fourth, it can be found from two point clouds that the SAM's dexterity becomes better in the outer workspace, while the PCW obtains better motion dexterity with the end effector closer to the central axis of the workspace. This result instructs the initial localization of the flexible endoscope before ESD.

From the above analysis, the HFMs are capable of rationally using the dexterity of different mechanical structures based on the requirements of surgical actions.

WORKSPACE

The SAM and PCW execute ESD in the endoscopic view. From the manufacturer specifications, the endoscope has a field of view (FOV) of 140° and a depth of view of [3, 100] mm. The workspace of the HFMs is acquired from the established kinematics models and is displayed at the endoscope tip in Figure 6(a). The workspace of the SAM and PCW presents a cylinder with a dome (SAM: about 37.8 mm in diameter, 48.6 mm in height; PCW: 30.1 mm in diameter, 46.4 mm in height). The precise workspace of the SAM and PCW is computed by the boundary function in MATLAB, at 44.1 and 21.2 cm^3, respectively. The SAM workspace is twice as large as the PCW workspace and almost covers it, which provides a large space to exert sufficient traction on tissue. Besides, for unreachable cutting points in the submucosal layer, the SAM can adjust the force and direction of the grasping point to deform the lesion to move the cutting point to the PCW workspace. From the top and side views, it can be found that the SAM and PCW can sweep areas with diameters of 38 and 30 mm, which means that both manipulators can cover lesions with diameters over 30 mm. Besides, both workspaces are almost contained within the endoscopic FOV (gray area), which guarantees the visual feedback of each manipulator's operation.

COOPERATION ANALYSIS

Bimanual manipulation requires effective cooperation among HFMs. The cooperative workspace is obtained by the intersection of the HFMs' workspaces, as in Figure 6(b). The cooperative workspace has a volume of 18.3 cm^3 (diameter in top view: about 30 mm, height: about 37 mm), which accounts for 41.37% of the SAM workspace and 86.08% of the PCW workspace. One of the HFMs' cooperative motions is illustrated at the left of Figure 6(c), and real practice can refer to Figure 1. The SAM can grasp one point of mucosa in its reachable workspace and pull the submucosa close to the PCW's tip in the cooperative workspace. Then, the PCW can execute dissection. Such a large cooperative workspace for the PCW can increase the dissection efficiency. Additionally, if the grasping point determined by the surgeon is outside the SAM workspace or causes the SAM's singularity (e.g., boundary points with $\mu^m = 52.52$), the PCW can hand it over to the SAM's forceps in the cooperative workspace, which is the other common cooperative motion of HFMs [see the right of Figure 6(c) and real practice in Figure 7(a)].

The HFMs' dexterity in the cooperative workspace plays an important role in motion execution. The dexterity distribution in the cooperative workspace is presented in Figure 6(c). The dexterity metric is divided into three zones: high, medium, and low, each of which occupies 30% of the whole dexterity range. The SAM's and PCW's high dexterity ranges are [3.6, 17.32] and [16, 32.7], respectively. Additionally, the HFMs' typical motions, illustrated in Figure 6(c), are exerted with high dexterity. For example, while the SAM ($q^m = [-2.8, 0, \pi/6, -pi/4, -pi/12]$) is grasping the mucosa with $\mu^m = 7.88$, the PCW ($q^w = [6, 0.3, -0.3]$) is performing submucosal dissection with $\mu^w = 17.87$. The HFMs' motions with high dexterity can make the cooperation more comfortable.

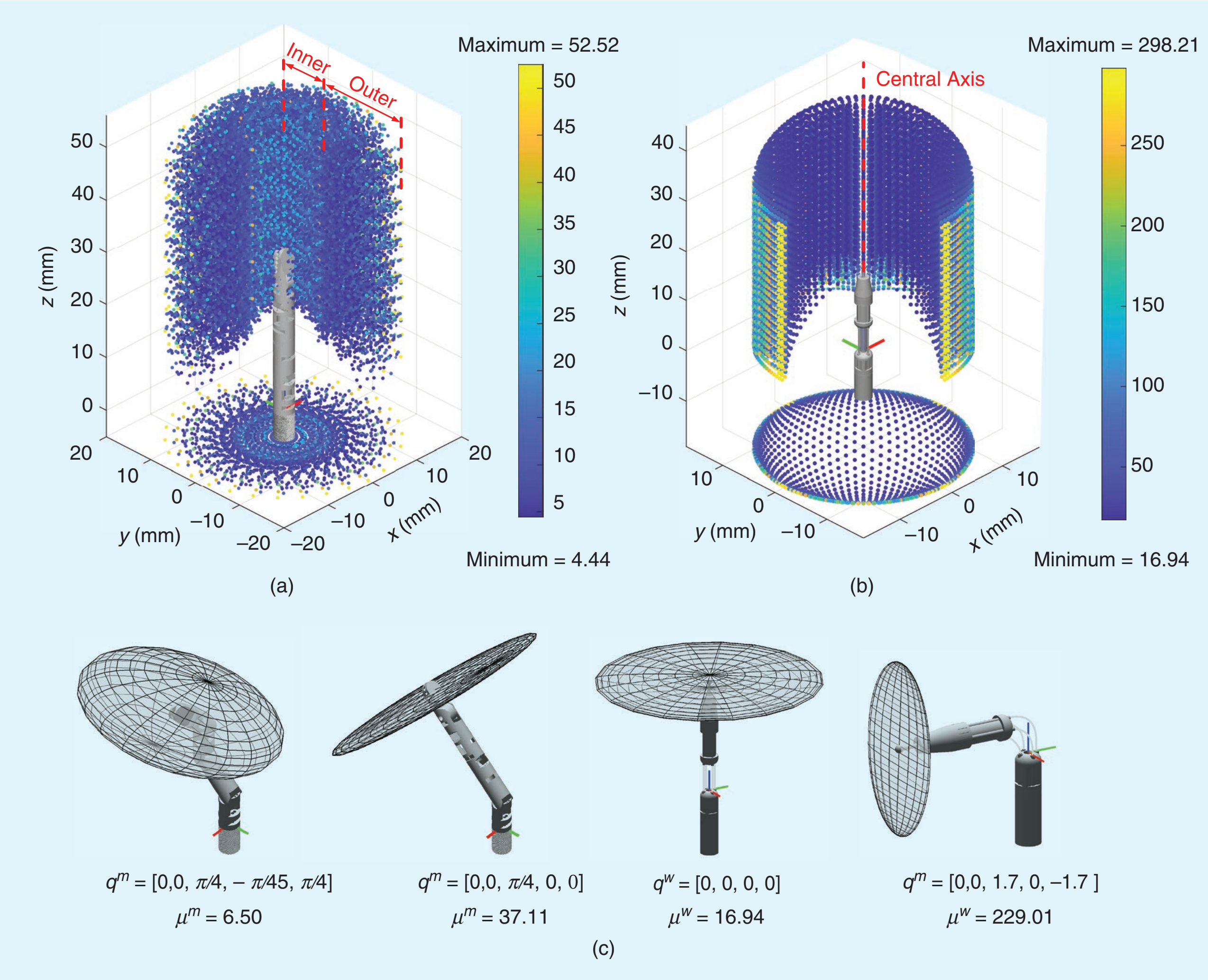

FIGURE 5. The linear motion dexterity analysis in the workspace. (a) The dexterity distribution of the SAM. (b) The dexterity distribution of the PCW. (c) Two manipulators' ellipsoids approaching extremum dexterity metrics μ^w, respectively.

IEEE Robotics & Automation Magazine (RAM) paper, presented at ICRA 2026, Vienna, Austria. Cite as RAM paper.

PERFORMANCE VALIDATION

In this section, we conduct ex vivo tests to validate the HFMs' performance. The transendoscopic telerobotic system is established as shown in Figure 8, which mainly consists of a surgeon console and a patient cart. The patient cart is stocked with electric hardware, including the HFMs' controllers, an imaging processor, a light source, and an electrosurgical unit, and equipped with robotic executors, including a 6-DoF robotic arm, HFMs, and a commercial dual-channel endoscope (Smart GS-60DQ, HUACO, China). The proximal handle of the endoscope and the HFMs' drivers are assembled on the end effector of the robotic arm to keep their relative position. The HFMs pass through two working channels (SAM/PCW through left/right channels) and reach the target position in the endoscopic view. The surgeon console is composed of two master hands (Robo, China), a foot pedal, and monitors displaying the endoscopic view and the HFMs' simulator [20]. The simulator is used to present the reference pose of the HFMs in real time based on the pose feedback of the master hands. The foot pedal is used to switch the functions of the PCW knife, including electric cutting and electrocoagulation.

To best replicate the human ESD environment in the ex vivo tests, we conduct five steps of preparation.

1) A pig stomach is chosen as the experimental target due to its similarity in anatomical structure and function to the human stomach.

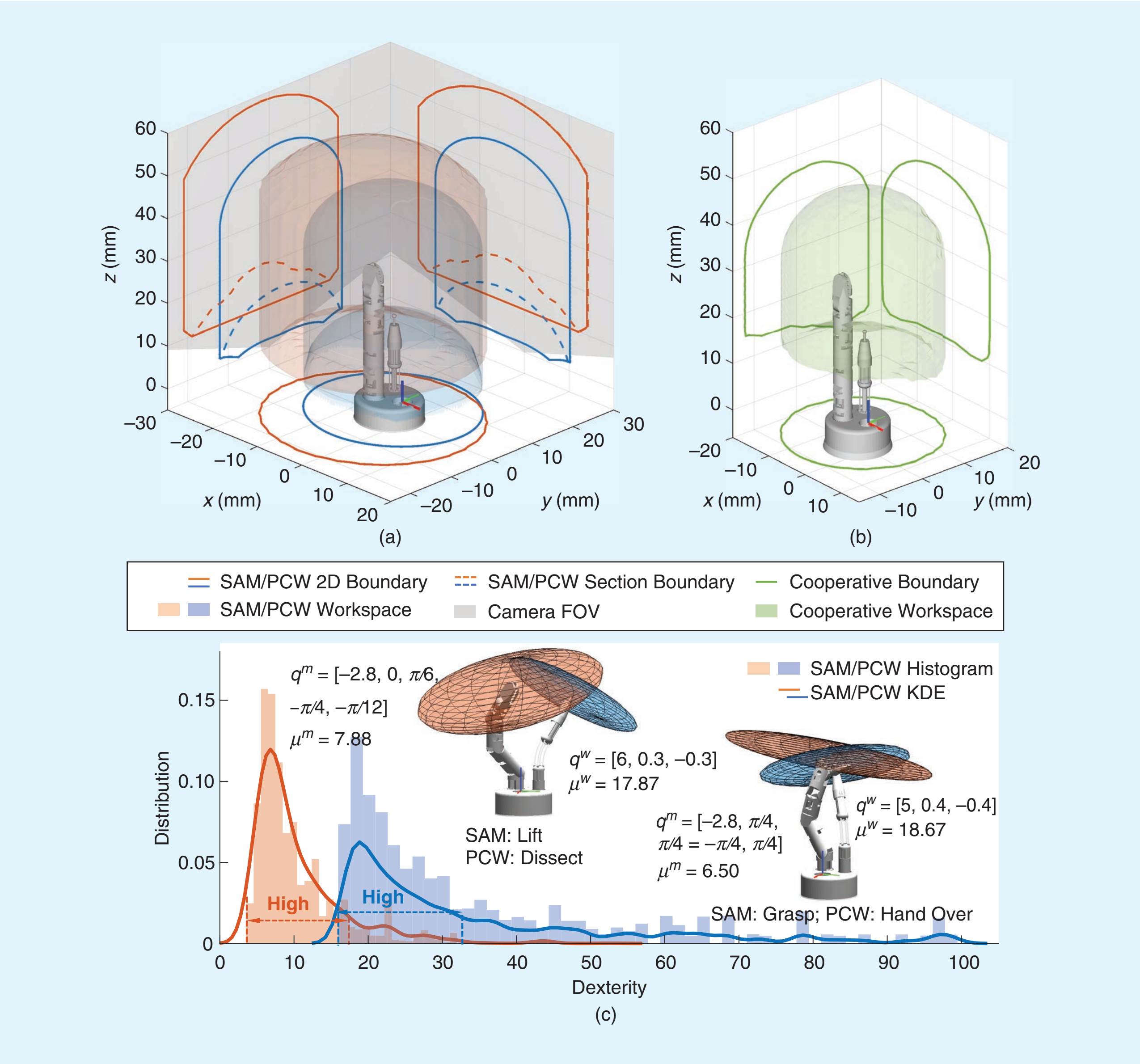

FIGURE 6. The workspace and cooperation analysis. (a) The reachable workspace of the HFMs in the endoscopic FOV. The boundaries of the central vertical section are drawn as dashed lines. (b) The cooperative workspace. Boundaries are plotted in green. The HFMs' models are shown inside the workspace. (c) The dexterity distribution in the cooperative workspace and typical cooperative motion simulation. Data with $\mu^w > 100$ are removed due to a low distribution.

IEEE Robotics & Automation Magazine (RAM) paper, presented at ICRA 2026, Vienna, Austria. Cite as RAM paper.

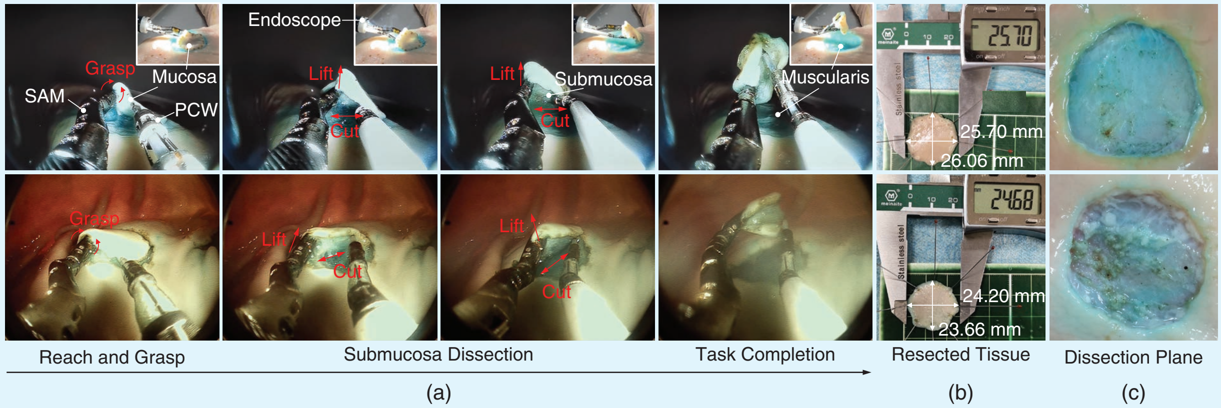

FIGURE 7. The ex vivo tests. (a) The ESD performance of the HFMs on everted (top) and inflated (bottom) stomachs. Endoscopic views depict the action sequence from left to right: reach and grasp → submucosal dissection → task completion. Red arrows indicate the motion direction of the SAM and PCW. For ESD on the everted stomach, side views are placed in the upper-right corners. (b) The resected specimens. The measurement results scaled because the vernier scale sometimes did not touch two sides of the mucosas tightly. (c) The dissection plane.

2) We use fresh pig stomachs daily and apply physiological saline during the ESD process to maintain the tissue elasticity as close as possible to the in vivo state.
3) Two environmental conditions with different difficulty levels are set up, as in Figure 7: everted stomach (easy) and inflated stomach (difficult). The latter is consistent with the real ESD environment on patients.
4) In both tests, the target areas are randomly selected on stomachs and created artificially through marking, injection, and circumferential dissection. The artificial lesions are circular areas with diameters of over 20 mm.
5) The operators are surgeons without ESD experience and endoscopic skills, who have just learned manipulation skills from the HFMs' simulator.

ESD ON AN EVERTED STOMACH

In this test, lesions are created on an everted gastric stomach. The HFMs are first inserted into the endoscopic working channels. Then, the endoscope tip is manually picked and placed behind the target lesion to keep it in the center of the endoscopic view. After this, the surgeon starts to teleoperate the HFMs to perform submucosal dissection, as demonstrated in Figure 7(a). The left SAM reaches and grasps the flap of the submucosal layer. While the SAM lifts the submucosal layer to provide a clear submucosal view, the right PCW slides along the submucosal layer with the electrosurgical unit activated to cut tissue simultaneously. The en bloc resection of the mucosa can be finished efficiently via the cooperation of the SAM and PCW. To validate the cooperative performance, we repeat robot-assisted ESD on nine lesions and acquire the statistical data in Table 3. The maximum size of the resected specimen, displayed in Figure 7(b), is 669.71 mm^2, and the mean size is up to 507.8 ± 88.03 mm^2. This is larger than the size requirement of the lesion (diameter >20 mm) for ESD. The mean dissection time and speed are 10.34 ± 4.01 min and 62.46 ± 41.85 mm^2/min (range: 26.63–154.10 mm^2/min), respectively. Among nine dissection planes [one appears in Figure 7(c)], three muscular injuries (33.33%) occur, and no perforation is observed. In conclusion, the HFMs can finish specific ESD actions efficiently and safely.

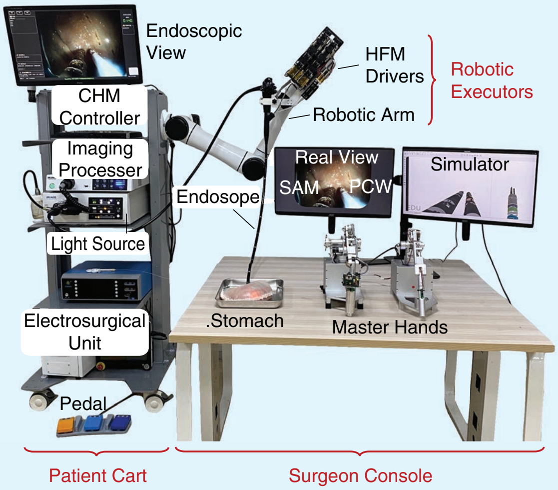

FIGURE 8. The transendoscopic telerobotic system and experimental setup. The system mainly includes a surgeon console and a patient cart equipped with robotic executors. The endoscope and HFMs are inserted into an ex vivo stomach to perform ESD procedures.

ESD ON AN INFLATED STOMACH

Initially, the artificial lesions are created inside the stomach, and then the stomach is inflated to provide a working workspace for the HFMs. Second, the endoscope is inserted into the inflated stomach, and then the HFMs pass through the working channels. Third, the endoscope is maneuvered manually (two distal bends by two handwheels and translation/

rotation by the endoscopic insertion part) to locate the target lesion. The operation process, as described in Figure 7(a), is identical to studies on the everted stomach. In the middle two endoscopic images, the SAM is lifting the tissue in different directions to expose the submucosa. Contrary to the everted condition, smoke tends to be generated by electrical cutting and has a serious impact on submucosal visualization. The surgeon has to pause the collaboration of the SAM and PCW and wait for the smoke suction and subsequent inflation by the endoscope. During these steps, the relative position between the endoscope and the target may be changed, so relocation should be executed by manually manipulating the endoscope. Seven tests are conducted, and the results are recorded in Table 4. The mean dissection time and speed slow to 11.95 ± 4.66 min and 41.1 ± 22.48 $\mathrm{mm}^2/\mathrm{min}$, respectively. The mean size of the resected specimens also reduces to 468.25 ± 232.27 mm^2 even though the maximum size goes up to 758.87 mm^2. The number of muscular injuries increases to four out of seven (57.14%), but no perforation happens. In conclusion, the working condition inside the inflated stomach tends to make ESD more difficult and less efficient because of the smoky view and unintuitive relocation via the endoscope, but the HFMs can still complete the most important task, submucosal dissection, of ESD.

ESD LEARNING CURVE

To validate the performance of the HFMs, we conduct a comparative study against traditional ESD performed on inflated

TABLE 3. The ESD on everted stomachs.

NUMBER	DISSECTION TIME* (MIN)	(LENGTH × WIDTH) SIZE† (MM^2)	DISSECTION SPEED (MM^2/MIN)	MUSCULAR INJURY/PERFORATION
1	13.07	(19.91 × 17.48) 348.03	26.63	Yes/no
2	11	(21.26 × 21.8) 463.29	42.12	No/no
3	13.67	(22.22 × 21.94) 487.45	35.67	Yes/no
4	4.83	(21.91 × 22.54) 493.85	102.18	No/no
5	15.85	(24.18 × 22.05) 533.06	33.63	Yes/no
6	11.95	(21.5 × 21.5) 462.28	38.68	No/no
7	10.07	(22.47 × 24.25) 544.89	54.13	No/no
8	8.93	(25.7 × 26.06) **669.71**	74.97	No/no
9	3.68	(23.34 × 24.32) 567.6	**154.1**	No/no
Mean	**10.34**	**507.8**	**62.46**	—
Standard deviation	**4.01**	**88.03**	**41.85**	—
Time‡	—	—	—	3/0

*The start time is the moment when the HFMs intend to perform submucosal dissection. The end time is the moment when the mucosa is fully resected.
†Size is equal to length × width.
‡Times present the number of injury and perforation.

TABLE 4. The ESD on inflated stomachs.

NUMBER	DISSECTION TIME (MIN)	(LENGTH × WIDTH) SIZE (MM^2)	DISSECTION SPEED (MM^2/MIN)	MUSCULAR INJURY/PERFORATION
1*	5.25	(20 × 10.25) 205	39.05	No/no
2*	9.13	(15.14 × 7.17) 108.55	11.89	No/no
3	16.67	(21.91 × 21.42) 469.31	28.16	Yes/no
4	12.5	(24.2 × 23.66) 572.67	45.81	No/no
5	18.83	(22.98 × 23.39) 537.39	28.53	Yes/no
6	9.2	(27.65 × 27.45) **758.87**	**82.49**	Yes/no
7	12.08	(27.24 × 22.98)	51.8	Yes/no
Mean	**11.95**	**468.25**	**41.1**	—
Standard deviation	**4.66**	**232.27**	**22.48**	—
Time	—	—	—	**4/0**

*The resected specimens after these two tests were not measured, and their sizes were estimated from videos.

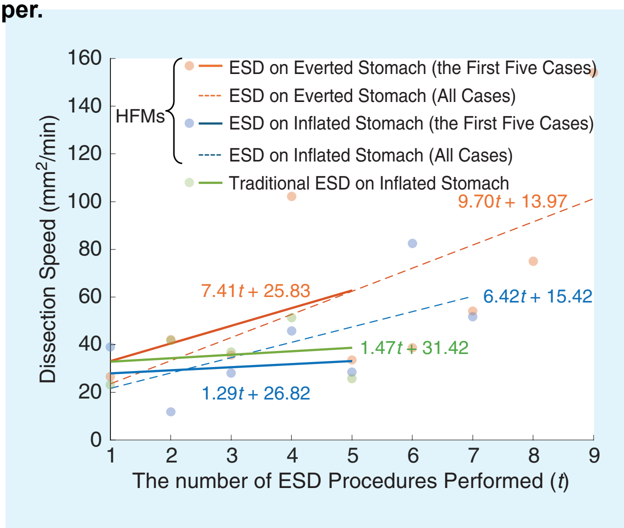

FIGURE 9. The ESD learning curves on three experimental conditions: robotic ESD on the everted stomach, robotic ESD on the inflated stomach, and traditional ESD on the inflated stomach. Solid and dashed lines indicate the first five cases and all cases, respectively.

stomachs. Besides the HFM-assisted ESD, one more surgeon without endoscopic skills and prior ESD experience performs five traditional ESDs. The average dissection speed (green points in Figure 9) is $35.83 \pm 11.6\ \mathrm{mm}^2/\mathrm{min}$, which is slightly slower than the HFM-assisted ESD on the inflated stomach. This demonstrates that our robotic system has potential for increasing ESD efficiency.

The sequences of robotic experiments follow the numbering in Tables 3 and 4. To align the experimental times, the first five cases of robotic ESD data and all data are plotted in Figure 9. The x-axis (time) represents the number of ESD procedures performed. All the learning curves are fitted by linear polynomial functions (the curve fitting toolbox in MATLAB). All the learning curves present a growing tendency. The curve slope can be defined as the learning speed (unit: $\mathrm{mm}^2/\mathrm{min}\cdot\mathrm{time}$). First, the learning speeds on everted stomachs are significantly faster than those on inflated stomachs, attributed to the easy endoscope positioning to the target in an open environment. More importantly, the HFMs' learning speeds range from 1.29 to 9.7 $\mathrm{mm}^2/\mathrm{min}\cdot\mathrm{time}$, which are closer to or higher than traditional ESD (1.47 $\mathrm{mm}^2/\mathrm{min}\cdot\mathrm{time}$). Furthermore, after five cases, they increase significantly, especially for ESD on inflated stomachs, rising from 1.29 to 6.42 $\mathrm{mm}^2/\mathrm{min}\cdot\mathrm{time}$. Although the limited data may result in significant variability in learning speeds, the above analysis demonstrates the feasibility of using our HFM-based robotic system to facilitate ESD training for novice surgeons.

CONCLUSIONS

In this work, we proposed the first HFMs combining a SAM and a PCW for bimanual ESD (flexibility). In detail, the SAM functions as maneuverable forceps for stable (stiffness) tissue traction along multiple directions (dexterity). The PCW is integrated with an electric knife for safe tissue dissection (accuracy). Each of the HFMs leverages its relatively better working properties to execute specific ESD actions. We used different modeling methods—the DH method for the SAM and the Cosserat rod model for the PCW—to establish kinematics and transform them to the endoscope space. Based on the design and kinematic modeling of the HFMs, a transendoscopic telerobotic system was built. Except for previously recorded properties (stiffness and accuracy), the dexterity and workspace of the HFMs were analyzed in detail via simulation. Finally, the feasibility of the HFM-based robotic system was validated by ESDs on both everted and inflated stomachs.

Currently, the robotic system is an original prototype, so further refinements are required for future work. First, the flexible endoscope is an essential part of the telerobotic system. We will develop a drive system for the endoscope to replace the manual control and incorporate its kinematics to construct an entire robotic kinematic model. Second, the passive section of the flexible endoscope was generally kept straight. We will investigate the impact of the endoscopic configuration on the HFMs' performance. Third, the performance validation of HFMs ended with a limited number of ex vivo tests, where the organs were static. We will carry out more comparative studies on in vivo stomachs and then conduct in vivo animal studies to validate the HFMs' performance in a dynamic environment.

ACKNOWLEDGMENT

This work was supported in part by CUHK Direct Grant for Research 2024/2025 [Grant 4055262 (HXG)], Young Talent Support Project of Guangzhou Association for Science and Technology [Grant QT-2025-046 (HXG)], Research Grants Council–Research Impact Fund [Grants R4020-22 and RIF R1007-24 (HLR)], NSFC Young Scientists Fund [Category A, Grant T252500134 (HLR)], and Research Grants Council–General Research Fund [Grants 14204524 (HLR and 14203323)]. Hongliang Ren is the corresponding author. This article has supplementary downloadable material available at https://doi.org/10.1109/MRA.2025.3616737, provided by the authors.

AUTHORS

Huxin Gao, Department of Electronic Engineering, Chinese University of Hong Kong, Hong Kong 999077, China. E-mail: huxingao@cuhk.edu.hk.

Xiaoxiao Yang, Department of Gastroenterology, Qilu Hospital of Shandong University, Jinan 250062, China. E-mail: yangxiaoxiao@mail.sdu.edu.cn.

Tao Zhang, Department of Electronic Engineering, Chinese University of Hong Kong, Hong Kong 999077, China. E-mail: tzhang@link.cuhk.edu.hk.

Xiao Xiao, Department of Electronic and Electrical Engineering, Southern University of Science and Technology, Shenzhen 518055, China. E-mail: x.xiao@ieee.org.

Changsheng Li, School of Mechatronic Engineering, Beijing Institute of Technology, Beijing 100081, China. E-mail: lics@bit.edu.cn.

IEEE Robotics & Automation Magazine (RAM) paper, presented at ICRA 2026, Vienna, Austria. Cite as RAM paper.

Max Q.-H. Meng, Department of Electronic Engineering, Southern University of Science and Technology, Shenzhen 518055, China; Department of Electronic Engineering, Chinese University of Hong Kong, Hong Kong 999077, China. E-mail: max.meng@ieee.org.

Xiuli Zuo, Department of Gastroenterology, Qilu Hospital of Shandong University, Jinan 250062, China. E-mail: zuoxiuli@sdu.edu.cn.

Yanqing Li, Department of Gastroenterology, Qilu Hospital of Shandong University, Jinan 250062, China. E-mail: liyanqing@sdu.edu.cn.

Hongliang Ren, Department of Electronic Engineering, Chinese University of Hong Kong, Hong Kong 999077, China. E-mail: hlren@ieee.org.

REFERENCES

[1] J. T. Maple et al., “Endoscopic submucosal dissection,” *Gastrointest. Endosc.,* vol. 81, no. 6, pp. 1311–1325, 2015, doi: 10.1016/j.gie.2014.12.010.

[2] K. Price et al., “Using robotics to move a neurosurgeon’s hands to the tip of their endoscope,” *Sci. Robot.,* vol. 8, no. 82, 2023, Art. no. eadg6042, doi: 10.1126/scirobotics.adg6042.

[3] L. Zorn et al., “A novel telemanipulated robotic assistant for surgical endoscopy: Preclinical application to ESD,” *IEEE Trans. Biomed. Eng.,* vol. 65, no. 4, pp. 797–808, Apr. 2018, doi: 10.1109/TBME.2017.2720739.

[4] G. Wang et al., “CoPESD: A multi-level surgical motion dataset for training large vision-language models to co-pilot endoscopic submucosal dissection,” 2024, *arXiv:2410.07540.*

[5] S. Atallah, A. Sanchez, E. Bianchi, and S. Larach, “Envisioning the future of colorectal surgery: preclinical assessment and detailed description of an endoluminal robotic system (ColubrisMX ELS),” *Tech. Coloproctol.,* vol. 25, no. 11, pp. 1199–1207, 2021, doi: 10.1007/s10151-021-02481-0.

[6] S. J. Phee et al., “Design of a master and slave transluminal endoscopic robot for natural orifice transluminal endoscopic surgery,” *Proc. Inst. Mech. Eng. Part C, J. Mechan. Eng. Sci.,* vol. 224, no. 7, pp. 1495–1503, 2010, doi: 10.1243/09544062JMES1880.

[7] F. Jelínek, E. A. Arkenbout, P. W. Henselmans, R. Pessers, and P. Breedveld, “Classification of joints used in steerable instruments for minimally invasive surgery—A review of the state of the art,” *J. Med. Devices,* vol. 9, no. 1, 2015, Art. no. 010801.

[8] M. B. Hong and Y.-H. Jo, “Design of a novel 4-DOF wrist-type surgical instrument with enhanced rigidity and dexterity,” *IEEE ASME Trans. Mechatron.,* vol. 19, no. 2, pp. 500–511, Apr. 2014, doi: 10.1109/TMECH.2013.2245143.

[9] C. Li, X. Gu, X. Xiao, C. M. Lim, and H. Ren, “Flexible robot with variable stiffness in transoral surgery,” *IEEE ASME Trans. Mechatron.,* vol. 25, no. 1, pp. 1–10, Feb. 2020, doi: 10.1109/TMECH.2019.2945525.

[10] A. Bajo and N. Simaan, “Hybrid motion/force control of multi-backbone continuum robots,” *Int. J. Robot. Res.,* vol. 35, no. 4, pp. 422–434, 2016, doi: 10.1177/0278364915584806.

[11] J. A. Childs and C. Rucker “A kinetostatic model for concentric push-pull robots,” *IEEE Trans. Robot.,* vol. 40, pp. 554–572, 2024, doi: 10.1109/TRO.2023.3327811.

[12] D.-Y. Lee et al., “Anisotropic patterning to reduce instability of concentric-tube robots,” *IEEE Trans. Robot.,* vol. 31, no. 6, pp. 1311–1323, Dec. 2015, doi: 10.1109/TRO.2015.2481283.

[13] C. B. Black, J. Till, and D. C. Rucker, “Parallel continuum robots: Modeling, analysis, and actuation-based force sensing,” *IEEE Trans. Robot.,* vol. 34, no. 1, pp. 29–47, Feb. 2018, doi: 10.1109/TRO.2017.2753829.

[14] C. E. Bryson and D. C. Rucker, “Toward parallel continuum manipulators,” in *Proc. IEEE Int. Conf. Robot. Autom. (ICRA),* Piscataway, NJ, USA: IEEE Press, 2014, pp. 778–785, doi: 10.1109/ICRA.2014.6906943.

[15] H. Gao et al., “Modeling and compensation of stiffness-dependent hysteresis for stiffness-tunable tendon-sheath mechanism in flexible endoscopic robots,” *IEEE Trans. Ind. Electron.,* vol. 71, no. 8, pp. 9328–9338, Aug. 2024, doi: 10.1109/TIE.2023.3314891.

[16] H. Gao et al., “Transendoscopic flexible parallel continuum robotic mechanism for bimanual endoscopic submucosal dissection,” *Int. J. Robot. Res.,* vol. 43, no. 3, pp. 281–304, 2024, doi: 10.1177/02783649231209338.

[17] C. Li et al., “A miniature manipulator with variable stiffness towards minimally invasive transluminal endoscopic surgery,” *IEEE Robot. Autom. Lett.,* vol. 6, no. 3, pp. 5541–5548, Jul. 2021, doi: 10.1109/LRA.2021.3068115.

[18] L. Cao et al., “Sewing up the wounds: A robotic suturing system for flexible endoscopy,” *IEEE Robot. Autom. Mag.,* vol. 27, no. 3, pp. 45–54, Sep. 2020, doi: 10.1109/MRA.2019.2963161.

[19] M. Hwang and D.-S. Kwon, “Strong continuum manipulator for flexible endoscopic surgery,” *IEEE/ASME Trans. Mechatron.,* vol. 24, no. 5, pp. 2193–2203, Oct. 2019, doi: 10.1109/TMECH.2019.2932378.

[20] H. Gao et al., “GESRsim: Gastrointestinal endoscopic surgical robot simulator,” in *Proc. IEEE/RSJ Int. Conf. Intell. Robots Syst. (IROS),* Piscataway, NJ, USA: IEEE Press, 2022, pp. 9542–9549, doi: 10.1109/IROS47612.2022.9982138.